

# **Two-Dimensional Flow Nanometry of Biological Nanoparticles for Accurate Determination of Their Size and Emission Intensity**

Stephan Block<sup>1\*</sup>, Björn Johansson Fast<sup>1</sup>, Anders Lundgren<sup>1,2</sup>, Vladimir P. Zhdanov<sup>1,3</sup>,  
Fredrik Höök<sup>1\*</sup>

<sup>1</sup> Division of Biological Physics, Department of Physics, Chalmers University of Technology, SE-412 96 Gothenburg, Sweden

<sup>2</sup> Department of Nanobiotechnology, University of Natural Resources and Life Sciences, 1190 Vienna, Austria

<sup>3</sup> Boreskov Institute of Catalysis, Russian Academy of Sciences, Novosibirsk 630090, Russia

Keywords: single particle tracking, nanoparticles, TIRF microscopy, size determination, microfluidics, data analysis

## **\*Corresponding authors:**

Prof. Dr. Fredrik Höök  
mail: fredrik.hook@chalmers.se  
Tel: +46 31 772 61 30

Dr. Stephan Block  
mail: stephan.block@chalmers.se,  
Tel: +46 31 772 33 67

## **Abstract**

Biological nanoparticles (BNPs) are of high interest due to their key role in various biological processes and use as biomarkers. BNP size and molecular composition are decisive for their functions, but simultaneous determination of both properties with high accuracy remains challenging, which is a severe limitation. Surface-sensitive microscopy allows one to precisely determine fluorescence or scattering intensity, but not the size of individual BNPs. The latter is better determined by tracking their random motion in bulk, but the limited illumination volume for tracking this motion impedes reliable intensity determination. We here show that attaching BNPs (specifically, vesicles and functionalized gold NPs) to a supported lipid bilayer, subjecting them to a hydrodynamic flow, and tracking their motion via surface-sensitive imaging enable to determine their diffusion coefficients and flow-induced drift velocities and to accurately quantify both BNP size and emission intensity. For vesicles, the high accuracy is demonstrated by resolving the expected radius-squared dependence of their fluorescence intensity.

## Introduction

Biological nanoparticles (BNPs) like viruses, exosomes, vesicles or biologically-functionalized particles are of high relevance for current research as they are involved in a multitude of processes (e.g., transmission of viral diseases<sup>1, 2</sup> and exosome-mediated cell-cell communication<sup>3, 4</sup>) or are promising candidates for novel therapeutic approaches (e.g., functionalized vesicles and NPs for targeted drug delivery<sup>5, 6</sup>). A full characterization of BNPs requires determination of their size as well as the amount of a particular biocompound (e.g., expression levels of surface proteins/markers on the NPs or DNA/RNA content carried by exosomes). The latter is accessible using appropriate staining procedures, allowing the compound of interest to be quantified based on the emitted fluorescence intensity.

For  $\mu\text{m}$ -sized objects like cells, flow cytometry has proven to be a versatile approach for such measurements.<sup>7</sup> Since their first introduction in 1953,<sup>8</sup> flow cytometers have been developed into sophisticated high-end tools for characterization of living cells based on their scattering and fluorescence intensity, allowing now up to 34 different cell parameters to be scrutinized.<sup>9</sup> However, direct application to smaller objects like BNPs remains challenging as the passage time across the detection region is too short to enable conversion of the weak scattering and fluorescence signals into a quantitative analysis of BNP size, optical density or biomarker content and, importantly, to make correlations between these parameters.<sup>10</sup>

During the past years, nanoparticle tracking analysis (NTA) has emerged as an attractive alternative to flow cytometry. By light-scattering and/or fluorescence imaging combined with the analysis of the Brownian motion of suspended sub-micron particles, high-precision size distributions of BNPs with radii smaller than 50 nm have been demonstrated.<sup>11</sup> However, since the position of randomly diffusing NPs with

respect to the illumination profile varies over time, scattering/fluorescence intensity signals are subject to large variations, causing disturbing fluctuations in plots correlating NP intensity and size.<sup>12</sup> Consequently, it is usually not possible to correlate NP size to optical density and/or specific biomolecular content on the single NP level.

In order to reach high accuracy in the determination of the fluorescence intensity emitted by BNPs, Stamou and co-workers developed an assay, in which fluorescently-labeled vesicles were immobilized at a glass interface and imaged using confocal microscopy.<sup>13</sup> This setup has the advantage that the BNPs are spatially fixed, allowing their intensity profile to be extracted with high reproducibility. Due to the immobilization, however, Brownian motion cannot be used to extract the BNP size distribution. Hence, two different fluorescent dyes generally have to be used for BNP characterization: one to extract the size distribution,<sup>13</sup> and one to detect the biomolecular compound of interest.<sup>14</sup> Furthermore, recent measurements from the same group cast doubts on the validity of extracting BNP sizes from the fluorescence intensity, since especially for small vesicles (diameter ~100 nm) large heterogeneities in the dye distribution among the vesicles were observed causing uncertainties in the size determination.<sup>15, 16</sup>

Accurate BNP characterization would therefore benefit from an approach that sufficiently restricts the BNP movement to allow for an accurate quantification of their emitted scattering or fluorescence intensity, while still permitting a Brownian movement, which can be used for accurate size determination. Herein, we describe such an approach, in which the BNPs of interest are linked to a fluid interface or, more specifically, the lipid bilayer supported at the bottom of a microfluidic channel, while the in-plane BNP movements are recorded using microscopy. Application of hydrodynamic forces on the BNPs induces their movement in flow direction, while the

movement perpendicular to the flow remains random, allowing the BNP size to be accurately determined by quantifying the deterministic and random components of the movement. The concept is demonstrated using different linking strategies, all being capable for restricting the movement in two dimensions while keeping the BNPs mobile, and on different BNPs (functionalized gold NPs and small unilamellar vesicles). Finally, high accuracy in the determination of BNP size and intensity is confirmed by clearly resolving the expected physical dependence between both parameters.

## RESULTS

### Theoretical considerations

All approaches reported so far (e.g., NTA) that determine NP size distributions using single particle tracking (SPT), exploit that the bulk diffusion coefficient  $D_b$  of spherical NPs (e.g., vesicles, exosomes etc.) within a viscous medium is connected to the hydrodynamic NP radius  $R$  by the Stokes-Einstein relation,<sup>17</sup>

$$D_b = \frac{k_B \cdot T}{6\pi \cdot \eta \cdot R}, \quad (1)$$

where  $k_B$  denotes the Boltzmann constant,  $T$  the absolute temperature, and  $\eta$  the dynamic viscosity. In such approaches, the random NP movement is tracked using microscopy and  $D_b$  is extracted for each recorded NP trajectory, allowing to create  $R$  histograms employing Equation 1. The measured NP trajectory is usually a two-dimensional (2D) projection of a 3D movement onto the focal plane of the microscope, as only those NPs can be tracked that are sufficiently close to the focal plane.

As shown in Supporting Section 1, the main source of random errors in such bulk-based size determination is given by the stochastic noise that is inherent to random walks and has a relative standard deviation  $\sigma_R / R$  given by

$$\frac{\sigma_R}{R} = \frac{\langle \Delta R^2 \rangle^{1/2}}{R} = \sqrt{\frac{2}{3} \cdot \frac{N_p}{N - N_p}}, \quad (\text{for } N_p \ll N) \quad (2)$$

where  $N$  denotes the number of frames of the analyzed track and  $N_p$  is the number of frames corresponding to the largest lag time ( $N_p \times \Delta t_0$ , with  $\Delta t_0$  denoting the time between 2 consecutive frames) used for the calculation of  $D_b$ . High accuracy in the determination of  $R$  therefore requires trajectories covering as many frames  $N$  as possible, which is limited, however, by the fact that a NP has to be sufficiently close to the focal plane to be trackable. The average track length can be estimated by (Supporting Section 1):

$$\langle N \rangle = \Delta t / \Delta t_0 = z_R^2 / 2D_b \Delta t_0, \quad (3)$$

where  $z_R$  denotes the Rayleigh length (*i.e.*, the length scale of the focal plane depth). Inserting typical values of commercial implementations ( $z_R \sim 5 \mu\text{m}$ , acquisition rate  $1 / \Delta t_0 = 30 \text{ fps}$ )<sup>18</sup> leads to an average trajectory length  $< 100$  frames for spherical NPs having  $R = 50 \text{ nm}$  ( $D_b = 4.4 \mu\text{m}^2/\text{s}$  in water at  $25^\circ\text{C}$ ) and therefore to measurement uncertainties exceeding 9% (Equation 2 with  $N_p = 1$ ) for  $R$ .

The random NP movement through the focal plane obviously limits the accuracy in bulk-based SPT. This can be avoided, however, by restricting the NP movement in 2D, *e.g.*, by linking them to fluid interfaces like a fluid-phase supported

lipid bilayer (SLB). This procedure keeps the NPs within the focal plane, thereby increasing the observation time and the accuracy in the measurement of NP properties (e.g., its 2D diffusion coefficient,  $D$ , as well as its fluorescence or scattering intensities; see Supporting Section 1). Such attempts, however, have not yet been successful for size determinations, as the NP's  $D$  value after linking is determined by the employed linkers and not by the NP's hydrodynamic size anymore, which is attributed to the high friction the linkers experience within the SLB.<sup>19</sup> Hence, the Stokes-Einstein relation, Equation 1, cannot be applied to extract  $R$  from  $D$ , as done in bulk-based approaches.

As shown here, this apparent shortcoming can be circumvented, if one studies linker-constrained 2D NP movement within a microfluidic channel, allowing to create a shear flow parallel to the SLB (Figure 1a). This generates a hydrodynamic shear force  $F_s$  acting on the NP in the direction of the flow, causing a NP drift in flow direction, while perpendicular to the flow the constrained movement remains random (Figure 1b). In theory, the NP  $D$  value and average velocity  $v_x$  in flow direction (denoted as  $x$ -axis in the following, see Figure 1b) are connected by the Einstein-Smoluchowski relation:<sup>17</sup>

$$\frac{D}{k_B \cdot T} = \frac{v_x}{F_s}. \quad (4)$$

This relation can be derived from the fluctuation-dissipation-theorem, which states that the forces, causing random fluctuations in the equilibrium state (here the random forces generated by the diffusing lipids interacting with the linker), also create a dissipation/friction if the system is subject to a non-random force (here the shear force creating a directed NP movement).<sup>20</sup> The derivation of Equation 4 implies that

the flow-induced motion of the SLB is negligible. This is the case provided that the channel flow rate is below a certain threshold value (approximately 100  $\mu\text{L}/\text{min}$  for the channel design shown in Figure 1),<sup>21</sup> otherwise Equation 4 should be complemented by additional parameters.<sup>22</sup> This constrain, however, creates no real limitation, since all flow rates used in this study are far below this threshold. It is also of interest that Equation 4 is applicable irrespective of the tiny mechanistic details of NP diffusion and force formation. In our case, as already mentioned,  $D$  is determined by the linker-lipid interaction, because for typical linkers the diffusion coefficient ( $< 1 \mu\text{m}^2/\text{s}$ )<sup>19, 23-25</sup> is much smaller than that for NP in bulk provided  $R$  is below 200 nm. In contrast, the value of the drift-inducing force is determined primarily by the NP-solution interaction, while the role of a linker is nearly negligible.

If  $v_x$  and  $D$  are extractable from NP trajectories, application of Equation 4 allows to directly calculate  $F_s$  acting on the particular NP. Furthermore, since this force depends on the NP hydrodynamic radius,  $F_s$  calculated from single trajectories should allow to determine  $R$ . We will in the following denote this interface-based approach as *2D flow nanometry*. If  $z$  denotes the coordinate perpendicular to the SLB (with the SLB interface at  $z = 0$  and  $z$  pointing towards the center of the channel), an analysis shows that  $F_s$  scales, in laminar flows, with the product of flow velocity at  $z = R$ , *i.e.*, at the middle of the NP<sup>21, 22, 26</sup> (provided the linker length is negligible), allowing us to write (Supporting Section 2)

$$F_s(R) = A \cdot \eta \cdot v_0 \cdot R \cdot (R + \lambda), \quad (5)$$

with  $A$  denoting a constant pre-factor (that accounts for the inhomogeneous flow profile around the NP),  $v_0$  the flow rate through the channel and the length  $\lambda$



specifying the solution behaviour just near the SLB-solution interface (this length is expected to be a few nm; in general, it may include the linker length above the SLB, but in our case this factor is negligible). Note that neither  $A$  nor  $\lambda$  depend on  $R$  and that both can be determined using calibration measurements (see next section). Consequently, Equation 5 can then be used generally to relate  $F_s$  (measured using Equation 4) and  $R$ , once the employed channel design has been calibrated.

### Calibration using well-defined gold NPs

To test the concept of NP size determination based on 2D flow nanometry, it is most convenient to analyse particles of well-defined size. This was done here using gold NPs, the size distribution of which had been determined by electron microscopy. The gold NPs were linked via streptavidin to biotin-conjugated lipids in the SLB (Figure 2a; see Materials and Methods section for details). Due to their high refractive index contrast to the surrounding liquid, SPT of SLB-linked gold NPs was done label-free using surface enhanced ellipsometric contrast (SEEC) imaging.<sup>27</sup>

Figure 1b shows typical trajectories of gold NPs ( $R \approx 30$  nm) measured for flow rates of 5, 10 and 15  $\mu\text{L}/\text{min}$ , respectively. Increasing the flow rate also increases the movement in the direction of the flow, which is well reflected in the  $x$ - and  $y$ -components of the trajectories (*i.e.*, in components parallel and perpendicular to the flow direction). While a predominantly linear increase of the  $x$ -position was observed (Figure 2b), indicating a directed movement in the flow direction, the movement along the  $y$ -axis indeed appeared to be purely random, as indicated by non-directed fluctuations of the  $y$ -position displaying no obvious trend (Figure 2c). The directed movement was, however, superimposed by fluctuations, causing minor deviations from a perfect linear increase in  $x$ -position over time (Supporting Figure 1). A stringent analysis revealed (Supporting Section 3) that  $v_x$  can be extracted from the

linear increase of the  $x$ -position, while  $D_x$  and  $D_y$ , *i.e.*, the 1D diffusion coefficients in the  $x$ - and  $y$ -direction, can be determined from the fluctuations of the  $x$ - and  $y$ -components, respectively. Since the SLB is a 2D isotropic medium  $D_x$  and  $D_y$  are expected to be equal, which is (within experimental error) observed for the gold NPs (Supporting Figure 2), demonstrating that the data extraction procedure successfully decouples the directed and random NP movements and allows calculating the 2D diffusion coefficient  $D$  (as an arithmetic average of  $D_x$  and  $D_y$ ) and  $F_s$  using Equation 4.

Furthermore, Equations 4 and 5 suggest that  $v_x$  scales linearly with  $v_0$  and  $D$ , which is consistent with our observations (Supporting Figure 3). Hence, after normalizing  $v_x$  by the applied flow rate  $v_0$ , all data points collapse onto a single master curve (red line in Supporting Figure 3d), allowing to quantitatively relate experiments performed at different  $v_0$  by regarding rather the normalized velocity  $v_x/v_0$  instead of  $v_x$  itself. Note that the noise in Supporting Figure 3 decreased with increasing  $v_0$ , which is attributed to the fact that higher flow rates induce larger NP displacements between consecutive frames. This in turn increases the signal to noise ratio in the measurement of  $v_x$ . Hence, the random error in the determination of  $F_s$  can be reduced by increasing  $v_0$  (as suggested in Supporting Section 1), an optimization strategy that is not supplied by bulk-based approaches.

As already noted, substituting  $v_x$  and  $D$  into Equation 4 makes it possible to directly extract  $F_s$  acting on each tracked NP. Figure 2d shows histograms of the normalized hydrodynamic force,  $F_s/v_0$ , measured for NPs having peak hydrodynamic radii of 30, 50 and 105 nm, exhibiting peaks in the  $F_s/v_0$ -distributions at 1.60, 4.05, and 10.83 fN/( $\mu$ L/min), respectively. These measurements allowed determining the calibration parameters  $A$  and  $\lambda$  of Equation 5 (Figure 2e, solid line), and therefore to calibrate the microfluidic channel for the determination of full size distributions.

This is further demonstrated in Figure 3 comparing size distributions obtained from 2D flow nanometry and electron microscopy (EM). Both methods yielded essentially the same distributions if a shift of 5 nm is taken into account, which is attributed to the PEG corona formed on the NP surface that is not resolvable in the EM images.<sup>28</sup> Repetition of such measurements indicated high reproducibility (Supporting Figure 4a). Additionally, linking the gold NPs specifically to transmembrane proteins (using an antibody-functionalized PEG corona as recently described by Johansson Fast et al.<sup>29</sup>) instead of using biotin-streptavidin-links did not affect the extracted distributions (Supporting Figure 4b), indicating also minor influence of the particular linking strategy.

### **Correlation of size and fluorescence intensity of small unilamellar vesicles**

For further validation of the proposed 2D flow nanometry approach, it was applied to analyze sub-100 nm vesicles (Figure 4). The vesicles (fluorescently labelled by incorporation of lissamine rhodamine-conjugated lipids) were linked to the SLB using cholesterol-conjugated DNA-tethers (Figure 4a) and tracked employing total internal reflection fluorescence microscopy (TIRFM), as previously described.<sup>19, 23</sup> A good agreement between the 2D flow nanometry size distributions and those obtained with NTA (Figure 4b) and dynamic light scattering (DLS, Figure 4c) was observed. Interestingly, while the NTA size distribution showed no vesicles with hydrodynamic radii below 25 nm (Figure 4b), such vesicles were resolved using 2D flow nanometry and DLS (Figure 4c). Further, the long tail in the NTA distribution, starting around 50 nm, is neither observed using 2D flow nanometry nor DLS.

In contrast to DLS, which does not offer single vesicle resolution, 2D flow nanometry and NTA allow information about vesicle size and fluorescence intensity to be extracted (Figure 5). However, the intensity traces extracted with these

methods differed considerably, which is attributed to the fact that in 2D flow nanometry the tracked vesicles remain within the focal plane during their passage through the field of view, leading to stable intensity traces (Figure 5a), while in NTA the vesicles were free to move in 3D and therefore continuously enter and exit the focal plane, leading to strong fluctuations of  $I$  (Figure 5b). Linking the vesicles to a fluid interface thus led to much better defined  $I$  values, which is well reflected in a plot of  $R$  versus  $I$  for both approaches (Figures 5c, d). In particular, the NTA data points (grey dots) showed strong fluctuations, making it impossible to resolve the expected scaling ( $I \propto R^2$ , solid line) in this parameter plot. For 2D flow nanometry (black dots), much lower fluctuations were observed and the expected scaling ( $I \propto R^2$ , solid line)<sup>30</sup> is clearly resolved, illustrating that maintaining vesicles in the focal plane during the whole measurement enables accurate determination of  $I$ .

## DISCUSSION AND CONCLUSION

A new approach was introduced for the size determination of NPs, which are linked to a fluid interface within a microfluidic channel. A shear force (generated by a channel flow) induced a directed NP movement, while the movement perpendicular to this shear force remained random. This allowed to directly extract the shear force acting on the NP and therefore its hydrodynamic size. The approach is versatile, which was demonstrated by successful application on inorganic (gold NPs) and biological NPs (fluorescent small unilamellar vesicles), using label-free detection based on SEEC imaging or TIRFM, respectively. In contrast to the well-established bulk NTA approach, linking confines the NP movement within the focal plane in 2D flow nanometry, enabling also accurate extraction of the emitted NP intensity.

The passage time through the field of view can be adjusted by the channel flow rate, thereby allowing optimizing the measurement accuracy. Other size-

determination approaches lack such an optimization strategy. The flow rate should be chosen in such a way that the distance travelled by the directed movement,  $v_x \cdot \Delta t_0$ , is larger than the square root of the mean squared displacement, *i.e.*,  $v_x > \sqrt{4 \cdot D / \Delta t_0}$ . As  $D$  is given by the diffusion properties of the linker (and not of the NP itself), which is typically on the order of  $1 \mu\text{m}^2/\text{s}$ , this suggests that  $v_x$  exceeds  $5 \mu\text{m}/\text{s}$  for typical acquisition rates of  $1 / \Delta t_0 \approx 10 \text{ fps}$ . Using Equation 4 this in turn indicates that the shear force acting on the NPs should be larger than  $25 \text{ fN}$ , a value which is independent of the NP size as it follows from the diffusive properties of the linkers and acquisition rate of the microscope. Referring back to Figure 2e, this shows that (in this study) a flow rate of  $15 \mu\text{L}/\text{min}$  is sufficient for NPs with  $R$  as small as  $20 \text{ nm}$ , which is far below the threshold to induce directed lipid movement in the SLB.<sup>21</sup>

Further, the field of view of the microscope used in this study ( $x$ -extension  $\sim 200 \mu\text{m}$ ) was large enough to track many of the gold NPs for at least 150 frames and most of the vesicles for at least 200 frames. The difference in these numbers is caused by the slightly lower  $D$  value of the vesicles due to the different linking strategy. This leads (Supporting Section 1, Equation 10) to expected relative random errors  $\sigma_R / R$  of 5% for the gold NPs, corresponding to a size accuracy of  $\pm 2 \text{ nm}$  for the gold NP batches in Figure 3c and 3d. These values seem to be reasonable since the size distributions extracted with 2D flow nanometry and electron microscopy are very similar and since the latter is known to offer nm-resolution for metal NPs.

For vesicles, the expected relative random errors are even lower with  $\sigma_R / R = 4\%$ , translating into  $\pm 1.5 \text{ nm}$  for the batches shown in Figure 5. Such high accuracies are indeed necessary to resolve the  $R$ - $I$  relationship (Figure 5c, d), since increased fluctuations would otherwise smear out the data points into a point cloud.

We therefore tried to suppress such fluctuations in NTA-derived  $R$ - $I$  plots by increasing the minimum number of frames required for trajectories to be included in the data analysis. This indeed reduced the fluctuations, but still did not permit to unambiguously resolve the expected  $R$ - $I$  relationship.

Motivated by Larsen et al.<sup>16</sup> we calculated the ratio of measured and expected intensity (Figure 5c, d; black dots versus solid line) in order to assess heterogeneities in dye-labeled lipid distributions across individual vesicles (Supporting Figure 5). The standard deviation of this ratio is 0.41 and 0.30 (for Figure 5c and 5d, respectively), which is lower than expected from Ref. 16, since the standard deviation increases with decreasing  $R$  and since Larsen et al. report similar values, although much larger vesicles (radii ranging between 50 nm and 400 nm) were used in their study.<sup>16</sup>

Note that the length  $\lambda$  in Equation 5, (connecting  $R$  and  $F_s$ ) was found to be important, since attempts to fit Equation 5 failed for  $\lambda = 0$ . In particular, the size distribution of the 30 nm gold NP batch was systematically overestimated, while the ones of the larger gold NP batches and all vesicle batches became systematically underestimated. The extracted  $\lambda$ -value of 24.4 nm is larger than expected, but on the same order of magnitude as in recent reports.<sup>31-33</sup>

In summary, our experiments have shown that the concept of 2D flow nanometry makes it possible to combine 2 different approaches, which seemed to be incompatible in the past, *i.e.*, sufficiently restricting the NP movement to allow for accurate measurements of NP emission, while still permitting them to obey a Brownian motion, which is required for accurate measurements of their size. Although so far demonstrated on two generic examples, application to other BNPs like viruses and exosomes appears to be feasible and marks the next steps.

## ONLINE METHODS

**Materials** – POPC (1-palmitoyl-2-oleoyl-sn-glycero-3-phosphocholine), DSPE-PEG(2k)biotin (1,2-distearoyl-sn-glycero-3-phosphoethanolamine-N-[biotinyl(poly(ethylene glycol))-2000] and rhodamine-DOPE (1,2-dioleoylsn-glycero-3-phosphoethanolamine-N-(lissamine rhodamine B sulfonyl)) were obtained from Avanti Polar Lipids Inc. (Alabaster, AL). Cholesterol-terminated DNA-strands were obtained from Eurogentec S.A. (Seraing, Belgium) with the following sequences: 5'-TGG-ACA-TCA-GAA-ATA-AGG-CAC-GAC-GGA-CCC-chol-3' ( $\alpha$ ); 5'-chol-CCC-TCC-GTC-GTG-CCT-3' ( $\alpha'$ ); 5'-TAT-TTC-TGA-TGT-CCA-AGC-CAC-GAG-TTC-CCC-chol-3' ( $\beta'$ ); 5'-chol-CCC-GAA-CTC-GTG-GCT-3' ( $\beta$ ). Tris(hydroxymethyl)-aminomethane hydrochloride (TRIS-HCl), sodium chloride and calcium chloride were obtained from Sigma Aldrich (Steinheim, Germany).  $\alpha$ -hydroxy- $\omega$ -mercapto-PEG,  $\alpha$ -carboxy- $\omega$ -mercapto-PEG and  $\alpha$ -biotinyl- $\omega$ -mercapto-PEG (all having 5 kDa) were purchased from RAPP Polymere (Tübingen, Germany). If not otherwise stated, all solutions were prepared or diluted using a TRIS-HCl buffer consisting of 100 mM Tris-HCl, 50 mM NaCl, 5 mM  $\text{CaCl}_2$  that was adjusted to pH = 7.4 using HCl.

**Vesicle Preparation** – Small unilamellar vesicles (SUV) were prepared by the extrusion method as described earlier,<sup>34</sup> or, alternatively, by sonication. Vesicles for SLB formation consisted of 99.8 mol% POPC and 0.2 mol% DSPE-PEG(2k)biotin and were extruded, while for single particle tracking two vesicle batches were created having a composition of 97 mol% POPC plus 3 mol% rhodamine-DOPE (sonicated; shown in Figure 5c), or of 98 mol% POPC plus 2 mol% rhodamine-DOPE (extruded; shown in Figure 5d). For extrusion, lipid films were formed in round bottom flasks under flowing nitrogen and dried in vacuum, hydrated by adding 1 mL of the Tris-HCl buffer, followed extruding the mixture through polycarbonate membranes

(Avanti Polar Lipids Inc., Alabaster, AL). Alternatively, to produce SUVs with different size distribution, these were formed by sonicating the lipid-buffer mixture (contained in a test-tube immersed in a ice-bath) using a tip sonicator for five times five minutes.

**Gold nanoparticles** – Gold NPs with a hydrodynamic radius of 30 nm were synthesized by seed mediated growth according to a modified version of the protocol presented by Park et al.<sup>35</sup>, using ascorbic acid as a reducing agent. The larger gold NPs were synthesized using the protocol presented by Perrault et al.<sup>36</sup> using hydroquinone as the reducing agent. Gold NPs were surface functionalized by chemisorption of thiolated poly(ethylene) glycol (PEG) ligands from a mixture of  $\alpha$ -hydroxy- $\omega$ -mercapto-PEG,  $\alpha$ -carboxy- $\omega$ -mercapto-PEG and  $\alpha$ -biotinyl- $\omega$ -mercapto-PEG in water solution. With the aim to modify each gold NP with a single biotinylated ligand, the relative content of  $\alpha$ -biotinyl- $\omega$ -mercapto-PEG in the mixture was adjusted for the different particle sizes in relation to their different surface areas. This was done assuming an approximate grafting density of  $1 \text{ nm}^{-2}$  (independent of NP size) for the different thiolated ligands, which means that for NPs with radius  $\sim 25 \text{ nm}$  and corresponding surface area  $\sim 8,000 \text{ nm}^2$ , the content of  $\alpha$ -biotinyl- $\omega$ -mercapto-PEG was 1/8,000 relative the total content of thiolated PEG in the mixture. After surface modification, NPs were purified from excess ligand by filtration using centrifuge filter columns with 300 kDa-cut off (PALL, USA). The gold NPs were further conjugated with streptavidin by adding gold NPs to a solution containing streptavidin in excess, followed by filtration as described above.

NP size distributions were determined by transmission electron microscopy (TEM). Electron micrographs were recorded on a FEI Tecnai G2 microscope operated at 160 kV acceleration voltage. The gold NP samples were applied on formvar and carbon-coated copper grids (FCF300-Cu-TB, Electron Microscopy Sciences, USA). These were hydrophilized by UV/Ozone treatment for 5 minutes



using an UV/Ozone ProCleaner from Bioforce Nanoscience and then further treated with poly-L-lysine (PLL), which was applied by positioning the grid up side down on a small droplet of PLL solution (20  $\mu\text{g/mL}$  in MilliQ water). Such-treated grids were coated with gold NPs by first positioning grids up-side-down on top of droplets with gold NP suspension (concentrated by centrifugation) for 15 minutes whereupon grids were blotted on a filter paper.

**TIRF-Microscopy** – Total internal reflection fluorescence (TIRF) microscopy was conducted on an inverted Eclipse Ti microscope (Nikon, Japan) that was equipped with a high-pressure mercury lamp, an Apo TIRF 60x oil objective (NA 1.49), and an Andor Neo CCD camera (Andor Technology, Belfast, Northern Ireland). A rhodamine filter set (TRITC, Semrock, Rochester, NY) was used, while focus drift was effectively reduced using the microscope's Perfect Focus System (PFS).

**SLB Formation and Vesicle Tethering** – All TIRF experiments were conducted on glass microscope coverslips as surfaces, which were supplemented with a home-made PDMS microfluidic channel (using the design as recently described<sup>21</sup>). SLBs were formed by injecting POPC vesicles (0.1 mg/mL, flow rate 20  $\mu\text{L/min}$  for 20 min), followed by rinsing with the Tris-HCl buffer (flow rate 20  $\mu\text{L/min}$  for 20 min). Vesicles were linked to a SLB using cholesterol-modified DNA strands as described earlier<sup>19, 23</sup>. SLBs and vesicles were incubated separately with 2 different types of DNA-strands, which carry a double-cholesterol group at one end that self-inserts the strands into the lipid bilayers. Both types of DNA-strands share a conjugated single-stranded part at the other end, which allows linking vesicles to the SLB via hybridization.

**Data Analysis** – All data analysis was done using home-made scripts written in MatLab (MathWorks, Natick, MA). Single particle tracking was implemented using local nearest-neighbor linking.<sup>37</sup> Diffusion coefficients were calculated using the

internal averaging procedure<sup>38</sup> on a moving window of the data points and corrected for motion blur<sup>39</sup>.

## ACKNOWLEDGEMENTS

The authors thank the Knut and Alice Wallenberg Foundation and the Swedish Research Council for funding.

## References

1. Barrow, E., Nicola, A.V. & Liu, J. Multiscale perspectives of virus entry via endocytosis. *Virology Journal* **10**, 177 (2013).
2. Mercer, J., Schelhaas, M. & Helenius, A. Virus entry by endocytosis. *Annual Review of Biochemistry* **79**, 803-833 (2010).
3. Denzer, K., Kleijmeer, M.J., Heijnen, H.F., Stoorvogel, W. & Geuze, H.J. Exosome: from internal vesicle of the multivesicular body to intercellular signaling device. *Journal of Cell Science* **113**, 3365-3374 (2000).
4. Valadi, H. et al. Exosome-mediated transfer of mRNAs and microRNAs is a novel mechanism of genetic exchange between cells. *Nature Cell Biology* **9**, 654-659 (2007).
5. Bareford, L.M. & Swaan, P.W. Endocytic mechanisms for targeted drug delivery. *Advanced Drug Delivery Reviews* **59**, 748-758 (2007).
6. Singh, R. & Lillard, J.W. Nanoparticle-based targeted drug delivery. *Experimental and Molecular Pathology* **86**, 215-223 (2009).
7. Shapiro, H.M. in *Practical flow cytometry*, Edn. 4th (Wiley-Liss., Hoboken, N.J.; 2003).
8. Coulter, W. Means for counting particles suspended in a fluid. U.S. Patent Nr. 2,656,508, 1953. (US; 1953).
9. Chattopadhyay, P.K. & Roederer, M. Cytometry: today's technology and tomorrow's horizons. *Methods* **57**, 251-258 (2012).
10. Orozco, A.F. & Lewis, D.E. Flow cytometric analysis of circulating microparticles in plasma. *Cytometry A* **77**, 502-514 (2010).
11. Dragovic, R.A. et al. Sizing and phenotyping of cellular vesicles using Nanoparticle Tracking Analysis. *Nanomedicine* **7**, 780-788 (2011).
12. Yang, D.T., Lu, X., Fan, Y. & Murphy, R.M. Evaluation of nanoparticle tracking for characterization of fibrillar protein aggregates. *AIChE* **60**, 1236-1244 (2014).
13. Kunding, A.H., Mortensen, M.W., Christensen, S.M. & Stamou, D. A fluorescence-based technique to construct size distributions from single-object measurements: application to the extrusion of lipid vesicles. *Biophys J* **95**, 1176-1188 (2008).
14. Mathiasen, S. et al. Nanoscale high-content analysis using compositional heterogeneities of single proteoliposomes. *Nat Methods* **11**, 931-934 (2014).
15. Elizondo, E. et al. Influence of the preparation route on the supramolecular organization of lipids in a vesicular system. *JACS* **134**, 1918-1921 (2012).
16. Larsen, J., Hatzakis, N.S. & Stamou, D. Observation of inhomogeneity in the lipid composition of individual nanoscale liposomes. *JACS* **133**, 10685-10687 (2011).
17. Einstein, A. Über die von der molekularkinetischen Theorie der Wärme geforderte Bewegung von in ruhenden Flüssigkeiten suspendierten Teilchen. *Annalen der Physik (Berlin)* **322**, 549-560 (1905).
18. van der Pol, E., Coumans, F.A., Sturk, A., Nieuwland, R. & van Leeuwen, T.G. Refractive index determination of nanoparticles in suspension using nanoparticle tracking analysis. *Nano Letters* **14**, 6195-6201 (2014).
19. Benkoski, J. & Höök, F. Lateral mobility of tethered vesicle - DNA assemblies. *Journal of Physical Chemistry B* **109**, 9773-9779 (2005).
20. Schwabl, F. & SpringerLink (Online service) in *Advanced quantum mechanics*, Edn. Third Edition. (Springer-Verlag Berlin Heidelberg; 2005).
21. Jönsson, P., Gunnarsson, A. & Höök, F. Accumulation and separation of membrane-bound proteins using hydrodynamic forces. *Analytical chemistry* **83**, 604-611 (2011).

22. Jönsson, P. & Jönsson, B. Hydrodynamic forces on macromolecules protruding from lipid bilayers due to external liquid flows. *Langmuir* **31**, 12708-12718 (2015).
23. Simonsson, L., Jönsson, P., Stengel, G. & Höök, F. Site-specific DNA-controlled fusion of single lipid vesicles to supported lipid bilayers. *Chemphyschem* **11**, 1011-1017 (2010).
24. Yoshina-Ishii, C. & Boxer, S.G. Controlling two-dimensional tethered vesicle motion using an electric field: interplay of electrophoresis and electro-osmosis. *Langmuir* **22**, 2384-2391 (2006).
25. Yoshina-Ishii, C. et al. Diffusive dynamics of vesicles tethered to a fluid supported bilayer by single-particle tracking. *Langmuir* **22**, 5682-5689 (2006).
26. Goldman, A., Cox, R. & Brenner, H. Slow viscous motion of a sphere parallel to a plane wall—II Couette flow. *Chemical Engineering Science* **22**, 653-660 (1967).
27. Gunnarsson, A., Bally, M., Jönsson, P., Medard, N. & Höök, F. Time-resolved surface-enhanced ellipsometric contrast imaging for label-free analysis of biomolecular recognition reactions on glycolipid domains. *Analytical chemistry* **84**, 6538-6545 (2012).
28. Lundgren, A. et al. Gold-nanoparticle-assisted self-assembly of chemical gradients with tunable sub-50 nm molecular domains. *Gold-nanoparticle-assisted self-assembly of chemical gradients with tunable sub-50 nm molecular domains* **31**, 209-218 (2014).
29. Johansson Fast, B. et al. (In manuscript; 2016).
30. Olsson, T., Zhdanov, V.P. & Höök, F. Total internal reflection fluorescence microscopy for determination of size of individual immobilized vesicles: Theory and experiment. *Journal of Applied Physics* **118** (2015).
31. Cross, B., Steinberger, A., Cottin-Bizonne, C., Rieu, J. & Charlaix, E. Boundary flow of water on supported phospholipid films. *Europhysics Letters* **73**, 390-395 (2006).
32. Leroy, S., Steinberger, A., Cottin-Bizonne, C., Trunfio-Sfarghiu, A. & Charlaix, E. Probing biolubrication with a nanoscale flow. *Soft Matter* **5**, 4997-5002 (2009).
33. Bonaccorso, E., Kappl, M. & Butt, H.J. Hydrodynamic force measurements: boundary slip of water on hydrophilic surfaces and electrokinetic effects. *Phys Rev Lett* **88**, 076103 (2002).
34. MacDonald, R.C. et al. Small-volume extrusion apparatus for preparation of large, unilamellar vesicles. *BBA* **1061**, 297-303 (1991).
35. Park, S., Yang, P., Corredor, P. & Weaver, M.J. Transition metal-coated nanoparticle films: vibrational characterization with surface-enhanced Raman scattering. *JACS* **124**, 2428-2429 (2002).
36. Perrault, S.D. & Chan, W.C. Synthesis and surface modification of highly monodispersed, spherical gold nanoparticles of 50-200 nm. *JACS* **131**, 17042-17043 (2009).
37. Meijering, E., Dzyubachyk, O. & Smal, I. in *Imaging and spectroscopic analysis of living cells: optical and spectroscopic techniques*, Vol. 504. (ed. P. Conn) 183-200 (Academic Press, 2012).
38. Saxton, M. Single-particle tracking: The distribution of diffusion coefficients. *Biophys J* **72**, 1744-1753 (1997).
39. Berglund, A. Statistics of camera-based single-particle tracking. *Phys Rev E* **82** (2010).

## Figure Captions

**Figure 1:** Framework for the size determination of nm-sized objects using 2D flow nanometry. **(a)** The objects (e.g., gold nanoparticles or liposomes) are linked to a fluid interface (e.g., a fluid phase supported lipid bilayer, SLB) within a microfluidic channel (using a design as recently described<sup>21</sup>). The linking confines the object's movement into 2 dimensions, but maintains its ability to move freely. Its movement is monitored from below, for example using scattering, confocal, or TIRF imaging. This is demonstrated in **(b)** for the particular example of streptavidin-functionalized gold nanoparticles (hydrodynamic radius 30 nm) that are linked to biotinylated lipids in the SLB and label-free monitored using SEEC imaging. Application of a flow through the channel creates a shear force, which depends on the flow rate (applied to the channel; 5  $\mu\text{L}/\text{min}$ , 10  $\mu\text{L}/\text{min}$ , and 15  $\mu\text{L}/\text{min}$  from top to bottom in **b**) and the object's hydrodynamic size. Shown are only the first 100 frames (= steps) of each trajectory corresponding to an observation time of 3 sec. The red trajectory is further analysed in Figure 2.

**Figure 2:** Calibration using well-defined gold nanoparticles (with a PEG shell thickness of 5 nm). Streptavidin-functionalized gold nanoparticles **(a)** that are linked to biotinylated lipids (linker length of approximately 5 nm) in the SLB and label-free monitored using SEEC imaging. **(b, c)** give a decomposition of a representative trajectory (30 nm gold nanoparticle; 15  $\mu\text{L}/\text{min}$  flow rate) into its component in flow direction ( $x$ -axis) and perpendicular to the flow ( $y$ -axis). Due to the flow, the  $x$ -component is dominated by a directed movement (indicated by its linear increase with time), allowing to extract the induced velocity  $v_x$ , while the  $y$ -component remains (due to absence of shear force in this direction) fully random and allows to extract the

linker diffusion coefficient  $D_y$  (see Supporting Section 3 for details). Combining both information yield the hydrodynamic shear force  $F_s$  acting on the particular nanoparticle. Histograms (**d**) of  $F_s$  (after normalization to the flow rate) exhibits a peak at 1.60 fN/( $\mu$ L/min) for 30 nm (blue), at 4.05 fN/( $\mu$ L/min) for 50 nm, and at 10.83 fN/( $\mu$ L/min) for 105 nm gold nanoparticles (hydrodynamic radius). These calibration measurements allowed to fit Equation 5 (**e**), which is required to convert distributions of the hydrodynamic force into size distributions. The solid line in **e** gives the result of a weighted LMS-fit that also takes the errorbars into account and yields  $\lambda = 24.4$  nm.

**Figure 3:** Comparison of size distributions of gold nanoparticle batches determined using electron microscopy (**a**, **c**) and using the novel 2D flow nanometry approach (**b**, **d**). The distributions are essentially identical and are only shifted by 5 nm, which is attributed to a 5 nm PEG corona formed on the surface of the gold nanoparticles that is not resolved in electron microscopy<sup>28</sup>.

**Figure 4:** 2D flow nanometry of small unilamellar vesicles, which were linked by cholesterol-equipped 13 nm DNA-tethers to the SLB (**a**). Comparison of vesicle size distributions obtained by NTA (**b**, grey curve), DLS (**c**, grey curve), and using 2D flow nanometry (**b** and **c**, black curve).

**Figure 5:** Comparison of vesicle intensity extraction done by 2D flow nanometry and NTA. (**a**) and (**b**) show representative intensity traces for a single, fluorescently labeled vesicles, while (**c**) and (**d**) compare the intensity-versus-size parameter plots obtained by NTA (grey dots) and 2D flow nanometry (black dots) for two different batches of small unilamellar vesicles. Both batches show peak hydrodynamic radii around 38 nm, but differ in their polydispersity. Due to much lower intensity

fluctuations observed in 2D flow nanometry (**a**) with respect to NTA (**b**), the expected scaling law is well visible in the parameter plots (solid lines in **c** and **d**), while it is hard to resolve for NTA data.

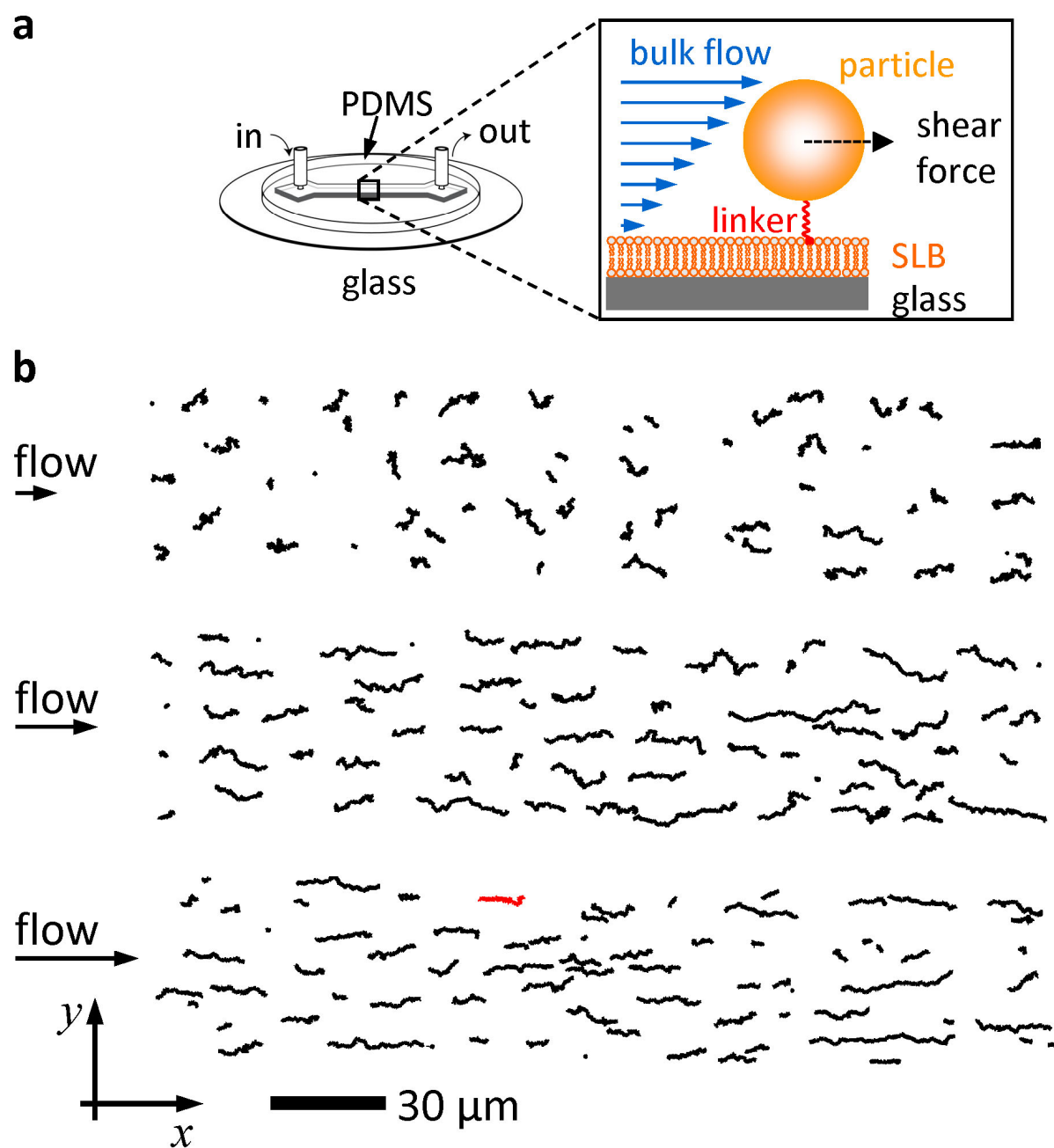


**Figure 1**



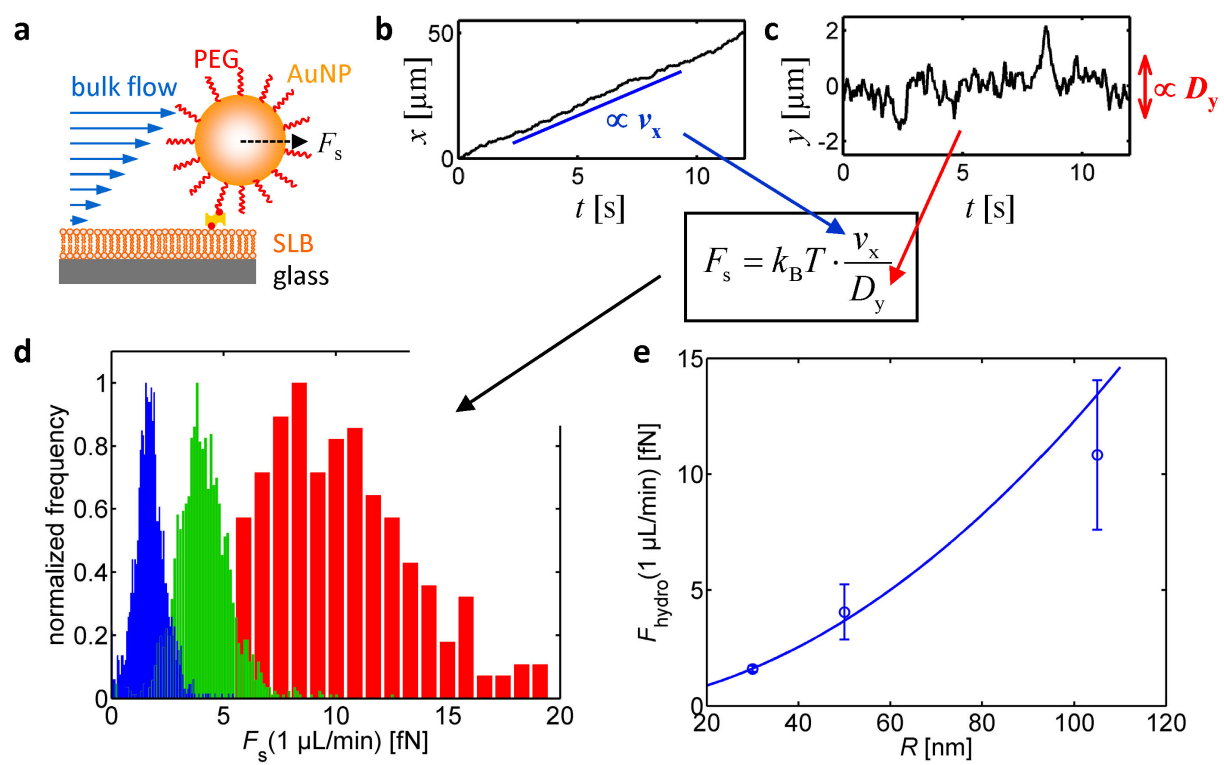


**Figure 2**

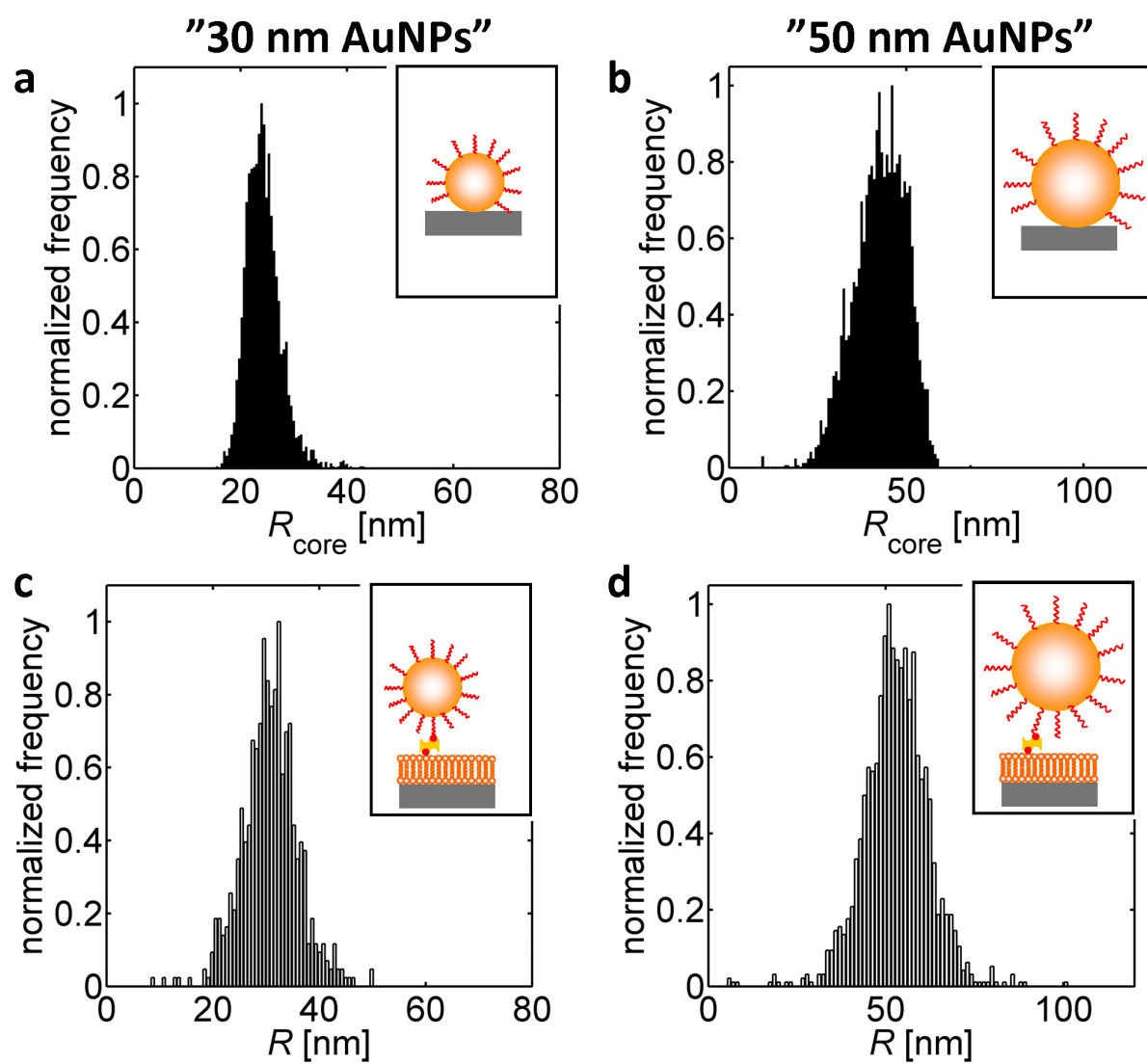


**Figure 3**

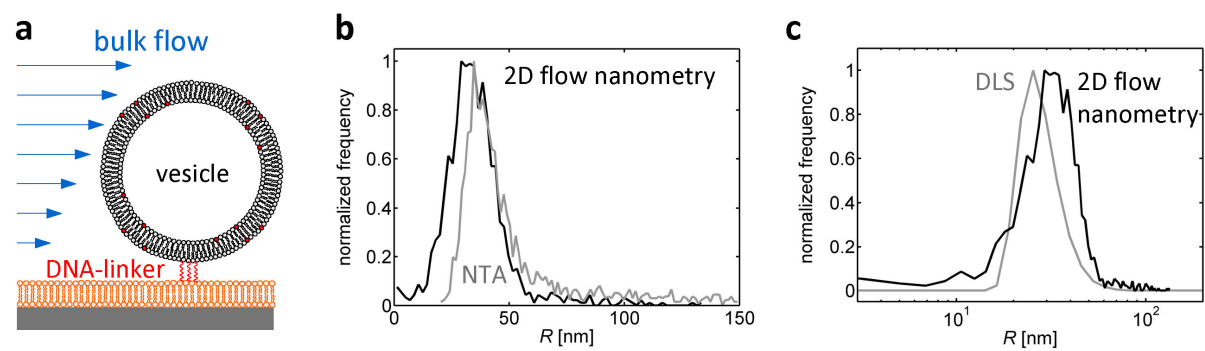


**Figure 4**

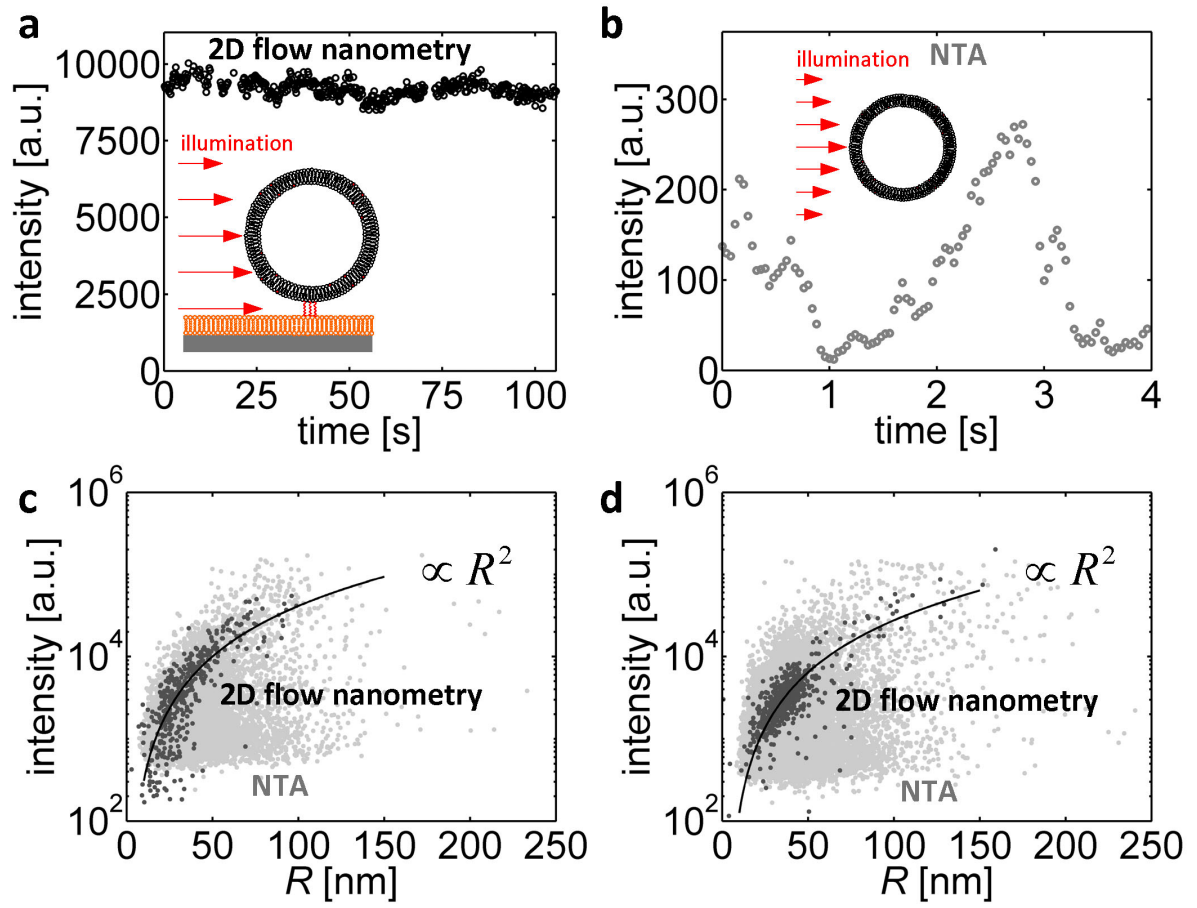


**Figure 5**